RSC Advances

PAPER

View Article Online
View Journal | View Issue

Cite this: *RSC Adv.*, 2026, **16**, 220

Comparative study of the peroxidase-like activity of copper(II) complexes with N_4 and N_2O_2 coordination environments. Application to the oxidation of phenol at moderate temperature

Joaquín Ferreyra,[a] Claudia Palopoli,[a] Nora Pellegri,[b] Gustavo Terrestre[a] and Sandra R. Signorella *[a]

The oxidation of phenol with H_2O_2 was investigated in the presence of mononuclear copper(II) complexes differing in the first coordination sphere, total charge, redox potential and/or geometry, under mild conditions. Among the tested complexes, $[Cu(py_2pn)]^{2+}$, where py_2pn = 1,3-bis(pyridin-2-ylmethyleneamino)propane, proved to be a good catalyst for the *para*-oxidation of phenol at 25 °C and neutral pH, while $[Cu(phen)_2]^{2+}$ shows the highest phenol conversion at pH 9. The kinetic study of H_2O_2 oxidation of phenol catalyzed by $[Cu(py_2pn)]^{2+}$ revealed that phenol oxidation strongly depends on pH and temperature and competes with H_2O_2 dismutation at high catalyst concentration, while overoxidation becomes significant at high pH and temperature. Increasing the temperature to 50 °C, noticeably improves phenol conversion but decreases regioselectivity. The comparison of the performance of the copper complexes with their manganese analogues, showed the copper complexes are better catalysts at 25 °C. Encapsulation of the cationic Cu(II) complexes into mesoporous SBA-15 silica by ion exchange allows for isolation of the complex within the pores avoiding the formation of the peroxo-diCu dimer through which the competitive H_2O_2 dismutation occurs and boosts the phenol conversion at room temperature.

Received 25th October 2025
Accepted 15th December 2025

DOI: 10.1039/d5ra08195e

rsc.li/rsc-advances

Introduction

Phenol is a key component and precursor of a large variety of fine chemicals, and its hydroxylation is an important industrial transformation.[1] However, the selectivity and efficiency of this conversion under mild conditions remains challenging.[2] H_2O_2 is a green reagent that provides a sustainable route to phenol hydroxylation with high atom efficiency.[3] However, although H_2O_2 is a potent two-electron oxidant ($E_{1/2}$ = 1.32 V *vs.* NHE, pH 7), it exhibits little activity due to the high activation energy of the kinetically controlled oxidation reactions, and, on the other hand, one-electron reduction renders H_2O_2 a rather weak oxidant ($E_{1/2}$ = 0.38 V *vs.* NHE, pH 7). Nevertheless, H_2O_2 overcomes these limitations acting as an efficient oxidant through the assisted activation by metalloenzymes[4–6] or transition metal complexes.[7,8] Inspired by copper-containing metalloenzymes, a number of copper-based complexes has been tested as functional peroxidase mimics.[9–12] In these reactions, the supporting ligand play a crucial role modulating the properties and catalytic activity, and the geometry around the copper centre might be critical for selectivity.[13] Besides, as H_2O_2 dismutation is another concern, the activation of H_2O_2 requires controlled conditions. A variety of Cu(II) complexes of open chain and cyclic ligands with N/O donor sites has been tested as catalysts for phenol hydroxylation using H_2O_2.[14–25] Although some of them have proven to be effective in hydroxylating phenol, these studies were done using different solvents, temperatures and pH. Therefore, since reaction conditions critically modify the catalytic phenol oxidation outputs,[26] the catalytic efficiency/selectivity of these systems cannot be directly compared, and key features behind catalyst reactivity remain elusive. In order to clarify structural factors affecting the oxidation of phenol by activated H_2O_2, it is important to obtain comparable results using the same reaction conditions. In this work, we evaluate phenol oxidation catalysed by four known Cu(II) complexes, $[Cu(phen)_2](ClO_4)_2$, $[Cu(phen)(OAc)_2]_2$-μ-OH_2], $[Cu(py_2pn)(ClO_4)_2]$ and [Cu(salpn)], where py_2pn = 1,3-bis(pyridin-2-ylmethyleneamino)propane and salpn = 1,3-bis(salicylidenamino)propane, under the very same experimental conditions, correlate their reactivity and structure in solution,

[a]*IQUIR (Instituto de Química Rosario), Consejo Nacional de Investigaciones Científicas y Técnicas (CONICET), Facultad de Ciencias Bioquímicas y Farmacéuticas, Universidad Nacional de Rosario, Suipacha 531, S2002LRK Rosario, Argentina. E-mail: signorella@iquir-conicet.gov.ar*

[b]*IFIR (Instituto de Física Rosario), Consejo Nacional de Investigaciones Científicas y Técnicas (CONICET), Facultad de Ciencias Exactas, Ingeniería y Agrimensura, Universidad Nacional de Rosario, 27 de Febrero 210 bis, 2000 Rosario, Santa Fe, Argentina*

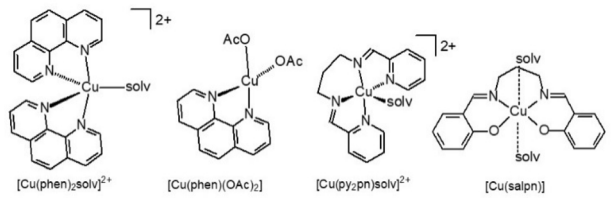

Fig. 1 Cu(II) complexes studied in this work.

and compare their activity with that of related Mn complexes. The structure of the four complexes in solution is shown in Fig. 1. Kinetic studies of phenol oxidation employing the best of these catalysts at low temperature, were performed and a suitable mathematic model was derived to describe the rate and mechanism of the reaction. Moreover, as a way to confine and isolate the catalyst to avoid the formation of peroxo-diCu dimers that lead to peroxide decomposition,[27] $[Cu(phen)_2]^{2+}$ and $[Cu(py_2pn)]^{2+}$ were incorporated into the channels of SBA-15 mesoporous silica particles by ionic exchange and the effect of encapsulation on the catalytic performance was assessed.

Experimental

Materials

The reagents used in this study were commercial products of the highest available purity and solvents were further purified by standard methods, as necessary. Complexes $[Cu(phen)_2](ClO_4)_2$, $[\{Cu(phen)(CH_3CO_2)_2\}(\mu\text{-}H_2O)]\cdot H_2O$, $[Cu(py_2pn)(ClO_4)_2]$ and [Cu(salpn)], were synthesized following previously reported procedures.[28–31] Synthetic details for the obtention of the four compounds are described in SI. Complexes $[Mn_2(py_2pn)_3](ClO_4)_2](ClO_4)_2\cdot 2H_2O$, $[Mn(3,5\text{-}Cl_2salpn)(H_2O)_2]ClO_4\cdot 2H_2O$, $[Mn(salpn)(H_2O)_2]ClO_4\cdot H_2O$, $[Mn(salpn)(\mu\text{-}O)]_2\cdot H_2O$, $[Mn(3,5\text{-}Cl_2salpn)(\mu\text{-}O)]_2$ used in the phenol oxidation screening assay were synthesized as previously described[32–34] and have correct analyses (given in SI).

Synthetic procedures

Mesoporous silica. SBA-15 silica was prepared by dissolving 4.08 g of pluronic P-123 copolymer in 1.6 M HCl (150 mL) at 35 °C. Then, 9 mL of tetraethyl orthosilicate (TEOS) were added and the mixture was left with stirring. After 20 h the temperature was raised to 85 °C and the mixture was stirred 24 h. The white solid was filtered and washed with distilled water several times, then dried in an oven at 60 °C for 18 h and finally calcined at 550 °C for 18 h, yielding 2.183 g of SBA-15.

Cu-py$_2$pn@SBA-15. A solution of $[Cu(py_2pn)(ClO_4)_2]$ (183 mg) in 60 mL of a 1 : 5 MeCN : MeOH mixture was slowly added on 313 mg of SBA-15 silica, and the resulting suspension was stirred at room temperature for 24 h. The solid was filtered, washed with MeOH until negative complex detection in the filtrate, and dried under vacuum. Yield: 278 mg. Anal. (wt%): Cu 0.22. Catalyst content: 3.4 mmol per 100 g. Significant IR bands (KBr, ν cm^{-1}): 2940 (w, ligand),1640 (δ, H–O–H), 1480 (w, ligand), 1450 (w, ligand), 1080 (ν_{as}, Si–O), 795 (ν_s, Si–O), 635 (w, ligand), 463 (δ, Si–O–Si).

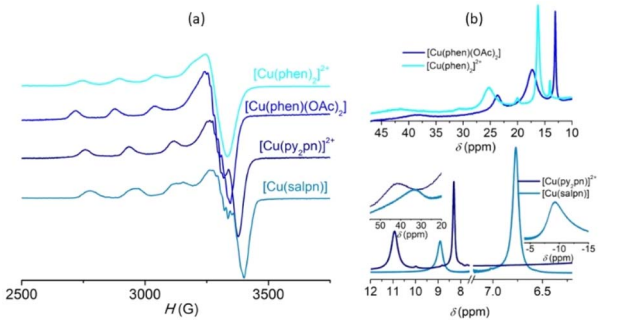

Fig. 2 (a) X-band EPR spectra of frozen DMF solutions of Cu(II) complexes, at 120 K. ν = 9.5 GHz. (b) ^{1}H NMR spectra of [Cu(salpn)] ($CDCl_3$), $[Cu(py_2pn)(ClO_4/DMSO)]^{+/2+}$ (D_6-DMSO), and $[Cu(phen)(OAc)_2]$ and $[Cu(phen)_2]^{2+}$ in D_3-MeCN.

Cu-(phen)@SBA-15. A solution of $[Cu(phen)_2](ClO_4)_2$ (185 mg) in 55 mL of a 1 : 5 MeCN : MeOH mixture was slowly added on 315 mg of SBA-15 silica, and the resulting suspension was stirred at room temperature for 24 h. The solid was filtered, washed with 1 : 10 MeOH : MeCN and MeOH until negative complex detection in the filtrate, and dried under vacuum. Yield: 275 mg. Anal. (wt%): Cu 0.08. Catalyst content: 1.3 mmol per 100 g. Significant IR bands (KBr, ν cm^{-1}): 2960 (w, ligand),1640 (δ, H–O–H), 1420 (w, ligand), 1080 (ν_{as}, Si–O), 795 (ν_s, Si–O), 463 (δ, Si–O–Si).

Analytical and physical measurements

UV-visible spectra were recorded on a Jasco V-550 spectrophotometer. Electron paramagnetic resonance (EPR) spectra were obtained at 115 K on an Elexsys E 500 Bruker spectrometer, operating at a microwave frequency of approximately 9.5 GHz. Metal content was determined with an inductively coupled plasma mass spectrometer (ICP-MS) PerkinElmer NexION 350×. CHN analyses were performed on a PERKIN ELMER 2400 series II Analyzer. Electrospray ionization (ESI) mass spectra were obtained with a UPLC-QTof Waters Synapt XS. The solutions for electrospray were prepared from solutions of complex diluted with methanol or MeCN to a final $\sim 10^{-5}$ M concentration. ^{1}H NMR spectra were recorded on a Bruker Avance III HD 400 MHz NMR spectrometer at ambient probe temperature (*ca.* 25 °C) and chemical shifts (in ppm) referenced to tetramethylsilane. Conductivity measurements were performed on 1.0 mM solutions of the complexes in MeCN, MeOH or DMF using a Horiba F-54 BW conductivity meter. The electrochemical experiments were performed with a computer-controlled Princeton Applied Research potentiostat, VERSASTAT II model, with the 270/250 Research Electrochemistry Software. Studies were carried out in a standard three electrode electrochemical cell under Ar, in acetonitrile (MeCN) solution using 0.1 M Bu_4NPF_6 as a supporting electrolyte and $\approx 10^{-3}$ M of the complex. The working electrode was a glassy carbon disk, and the reference electrode was a calomel electrode isolated in a fritted bridge with a Pt wire as the auxiliary electrode. Under these conditions, E(ferrocene/ferrocenium) = 388 mV in MeCN,

at room temperature. HPLC-UV measurements were performed on a Dionex-Thermo Scientific Ultimate 3000 RSLC chromatograph with UV-Vis VWD-3400RS detector, using the following conditions: isocratic mobile phase H_2O : acetonitrile (50 : 50)/0.1% formic acid, 0.8 mL min^{-1}, column Luna C18, Phenomenex (250 × 4.6 mm; 5 μm particle size), 35 °C. Under these experimental conditions, retention times t_R were as follows: phenol (t_R = 5.47 min), *p*-benzoquinone (t_R = 4.65 min), catechol (t_R = 4.09 min), hydroquinone (t_R = 3.52 min). Transmission electron microscopy (TEM) analysis was performed with a TEM/STEM JEM 2100 Plus with the operational voltage of 200 kV (variable), with a LaB6 filament. The samples were prepared by placing a suspension of silica and hybrid samples in ethanol onto a square mesh copper grid (400 mesh), coated with a layer of Formvar and carbon. The suspension of material in ethanol was left to dry, evaporating the ethanol, leaving the dispersed particles to adhere to the Formvar/Carbon surface. N_2 adsorption–desorption isotherms were obtained at 77 K on a Micrometric ASAP 2020 V4.02 (V4.02 G) apparatus.

Crystallography

Crystallographic data for compounds $[Cu(phen)_2(MeCN)](ClO_4)_2$, $[Cu(phen)_2Cl]ClO_4$ and $[\{Cu(phen)(OAc)_2\}_2$-μ-$H_2O]$ were collected at 298(2) K on a Bruker D8 QUEST ECO Photon II CPAD Diffractometer, using graphite monochromated Mo-Kα radiation (λ = 0.71073 Å). Data collection was carried out using the Bruker APEX4 package,[35] and cell refinement and data reduction were achieved with the program SAINT V8.40B.[36] The structure was solved by direct methods with SHELXT V 2018/2 (ref. 37) and refined by full-matrix least-squares on F^2 data with SHELXL-2019/1.[38] Molecular graphics were performed with ORTEP-3,[39] with 50% probability displacement ellipsoids. Crystal data collection and refinement parameters for the three compounds are summarized in Table S1, and selected bond distances and angles are listed in Table S2. Crystallographic data for $[Cu(phen)_2(MeCN)](ClO_4)_2$, $[Cu(phen)_2Cl]ClO_4$ and $[\{Cu(phen)(OAc)_2\}_2$-μ-$H_2O]$ have been deposited at the CCDC under CCDC-2495739, CCDC-2495740 and CCDC-2495857, respectively.

Stability measurements

The stability of the complexes was verified spectrophotometrically in the media used for the kinetic studies, mixtures of buffer (pH 7 or 9), acetone, DMF or MeCN, during 2 h. In all cases no changes were observed in the 250–900 nm spectral region, indicating the stability of the complexes in the experimental conditions of the kinetic essays.

Kinetic measurements

Homogeneous phenol oxidation. The oxidation of phenol by H_2O_2 in the presence of excess of 4-aminoantipyrine (4-AAP) catalysed by different complexes, was monitored at 500 nm, at fixed pH and temperature. The reaction yields were quantified based on the molar absorption coefficient of the *p*-quinoneimide adduct at 500 nm determined through the complete oxidation of phenol with commercial peroxidase enzyme, in the same reaction media used in the tests: ε^{500} (M^{-1} cm^{-1}): 7290 (5 : 1 buffer phosphate pH 7 : MeCN); 5900 (5 : 1 buffer phosphate pH 7 : DMF); 10600 (5 : 1 buffer borate pH 9 : DMF). In all cases, phenol : H_2O_2 : 4-AAP blanks were measured in the same solvent used to monitor the catalytic reaction and were subtracted from the reaction mixtures. Measurements at pH 9 were only done in DMF:buffer mixtures to avoid phenol oxidation by the MeCN-H_2O_2 adduct, the formation of which is favoured in basic medium.[40] In a typical experiment, 10 μL of a 0.99 M H_2O_2 in acetone were added to 2.5 mL of buffer solution (pH 7 or 9) containing 0.8 μmol of phenol and 2.04 μmoles of 4-AAP. H_2O_2 solutions were prepared in acetone where the formation of 2-hydroxy-2-hydroperoxypropane stimulates gradual availability of the oxidant, avoiding its decomposition. The reaction started with the addition of 0.5 mL of a 0.016 mM catalyst (1% of [phenol]) in DMF or MeCN, and left to react with stirring during 2 h.

For H_2O_2 phenol oxidation catalysed by $[Cu(py_2pn)]^{2+}$, the $[4\text{-AAP}]_0$ = 0.68 mM in all the kinetic runs, and the $[catalyst]_0$, $[phenol]_0$ and $[H_2O_2]_0$ were varied between 0–53 μM, 0.05–4 mM and 0.17–17 mM, respectively, at pH 7 and 9, and at T = 25 °C and 50 °C. Reactions were followed at 500 nm during 2 h, and initial rates were determined by non-linear square-fit of data. All experiments were done by duplicate and the calculated rates were within 5% of each other. The raw data of the time-course of absorbance change at 500 nm for the kinetic study of H_2O_2-based phenol oxidation catalysed by $[Cu(py_2pn)(ClO_4)_2]$ are available in the UNR Repository of Academic Data.[41] A kinetic model describing the rate law for *p*-quinoneimide formation was fitted to the whole set of experimental data simultaneously, at each pH and temperature condition in R,[42] using the nlsLM() function from the minpack.lm package.[43] Model selection was based on the Akaike Information Criterion (AIC) and the Bayesian Information Criterion (BIC), as well as on residual analysis.

Phenol oxidation with immobilized catalysts. 1.5 mg of Cu-py_2pn@SBA-15 or Cu-phen@SBA-15 were suspended in 2 mL of pH 9 buffer and added to a solution of 1.6 μmol of phenol in 4 mL pH 9 buffer. The reaction started with the addition of 20 μL of a 0.99 M H_2O_2 in acetone, and the resulting mixture was stirred during 2 h. The final concentrations of reagents were: [phenol] = 0.27 mM, $[H_2O_2]$ = 3.3 mM, catalyst@SBA-15 = 25 mg/100 mL. Then the mixture was centrifuged at 6000 rpm during 5 min. The supernatant was separated and the solid washed with 1 mL buffer and centrifuged. To the combined liquids, 270 μL of 2.04 mM 4-AAP solution, 15 μL of 0.21 M H_2O_2 in acetone and a volume of horseradish peroxidase (200 UI mL^{-1}) necessary to complete the dilution of the initial liquid to one-fifth, were added. The reaction catalysed by the enzyme was monitored at 500 nm until complete conversion of the remaining phenol. The reaction with each material was done in triplicate. As a control assay, SBA-15 without catalyst was used employing identical reagent concentrations and procedure as with the functionalized silica, and the measured turnover number (TON) was subtracted from that with the catalyst.

Results and discussion

Four Cu(II) complexes, formulated in the solid state as $[Cu(phen)_2](ClO_4)_2$, $[\{Cu(phen)(OAc)_2\}_2$-μ-$H_2O]$, [Cu(salpn)], and

$[Cu(py_2pn)(ClO_4)_2]$, that differ in the primary coordination sphere (N_4 or N_2O_2), total charge and degree of geometrical distortions around the metal ion, were selected to compare them as catalysts for phenol oxidation by H_2O_2. Even when these compounds are known, and their structures well defined in crystalline solids, it is known that either geometry or even composition and nuclearity may be different in solution. Therefore, the structure of the four complexes was examined in solution.

Complex $[Cu(phen)_2](ClO_4)_2$ was obtained from reaction of a 1.4 : 1 phen : $Cu(ClO_4)_2$ mixture in water under reflux. In this complex, Cu(II) is bound to the N_4-donor set of two phen ligands and it was reported that it adopts a compressed tetrahedral structure.[44] In solution, the metal centre of this compound most likely coordinates the solvent to form the pentacoordinate complex, as observed when $[Cu(phen)_2](ClO_4)_2$ dissolves in acetonitrile to give $[Cu(phen)_2(MeCN)](ClO_4)_2$, whose crystal structure was obtained by slow evaporation of a MeCN solution of $[Cu(phen)_2](ClO_4)_2$ (Fig. S1(a)). The molecular structure of this complex shows that the Cu(II) ion is bound to a N_5-donor set, one N-atom from acetonitrile, and two pairs of N-atoms from the two phen ligands. The calculated distortion index τ_5 = 0.92 (τ_5 = 0 for a perfect tetragonal geometry, and 1 for a perfectly trigonal-bipyramidal geometry),[45] denotes the Cu(II) ion is located in a distorted trigonal bipyramidal geometry, with the N-atom from acetonitrile and two N-atoms of two phen ligands in the trigonal plane, and the other two N-atoms from the two phen ligands occupying the axial positions. Even when this structure is somewhat different from that previously reported for crystals formed by slow diffusion of an acetonitrile/diisopropylether solution at room temperature,[46] it is evident that in a coordinating solvent, the fifth position can be occupied. Additionally, crystals of $[Cu(phen)_2Cl]ClO_4$ (Fig. S1(b)) grew by slow evaporation from a basic aqueous solution (pH 9) of $[Cu(phen)_2](ClO_4)_2$ (buffer borate prepared from boric acid, sodium borate and potassium chloride mixture), a medium used for the kinetic measurements described below. In this case, the calculated distortion index for the $CuClN_4$ coordination geometry is τ_5 = 0.8, denoting a more distorted trigonal bipyramid with chloride in the equatorial plane. The structure of this complex is similar to that reported by Boys *et al.*,[47] slightly different from that of the hemihydrate obtained by slow evaporation of an aqueous solution of $Cu(phen)_2Cl_2$ + $NaClO_4$,[48] and well different from the mono-hydrated triclinic complex crystallized from the mother liquor of $CuSO_4$ + phen reaction mixture in basic aqueous solution and ethanol.[49] In the monohydrate, the geometry around the Cu(II) ion is a much more distorted trigonal bipyramide having a square based pyramidal distortion (τ_5 = 0.68).

The reaction of a 1 : 1 ratio of phen and $Cu(OAc)_2$ in ethanol/acetone, affords the dimer $[\{Cu(phen)(CH_3CO_2)_2\}_2$-μ-$H_2O]$, where two $Cu(phen)(OAc)_2$ moieties are bridged by one water molecule (Fig. S1(c and d)). This dimer is analogous to that previously reported for the complex formed using a 2 : 1 phen : $Cu(OAc)_2$ ratio, in acetonitrile[50] or neat ethanol.[51] In $[\{Cu(phen)(CH_3CO_2)_2\}_2$-μ-$H_2O]$, each Cu(II) ion is bound to a O_3N_2-donor set from two acetate, one phen and one water molecule. The calculated distortion index τ_5 = 0.21, denotes the Cu(II) ion is located in a distorted square pyramidal geometry[45] with the water molecule placed at the apical position, and, as it is described below, in solution the dimer dissociates but the geometry around the Cu(II) ion is preserved.

$[Cu(py_2pn)(ClO_4)_2]$ crystallized by slow diffusion of ether into an acetonitrile solution of the complex.[27] In the crystal, the ligand is disposed in the equatorial plane with the two perchlorate anions occupying the apical positions. In solution, one of the perchlorate anions dissociates and the complex adopts a distorted square pyramidal geometry with perchlorate (τ_5 = 0.23) or a solvent molecule (τ_5 = 0.33, solvent = DMF, calculated from data reported in ref. 27) placed at the apex. Dissociation of the second perchlorate anion in protic solvents was confirmed by conductivity measurements of the complex in methanol, where the major species is $[Cu(py_2pn)(MeOH)]^{2+}$.

[Cu(salpn)] was obtained from a 1 : 1 mixture of $Cu(OAc)_2$ and H_2salpn in methanol. The crystal structure of this complex has been reported as a tetrahedrally distorted square-planar complex with Cu(II) bound to the N_2O_2-donor set of the ligand, where the dihedral angle between the CuNO planes is 25.4°.[52,53] The λ_{max} of the d–d transition band of this complex is observed at 605 nm in toluene,[52] the same wavelength as that in ethanol[54] or acetonitrile described below indicating the retention of the geometry around the Cu(II) ion in solution independently of the solvent.

The ESI-mass spectra of the complexes show that, in each case, the basic structural units are retained in solution (Fig. S2–S5), and the major species observed in the ESI-mass spectra are: $[Cu(phen)_2]^{2+}$ (m/z = 211.5, 100%); $[Cu(phen)(OAc)]^+$ (m/z = 302, 100%); $[Cu(py_2pn)]^+$ (m/z = 315.1, 100%) and $[Cu(py_2pn)(ClO_4)]^+$ (m/z = 414, 30%); and $[Cu(salpn)]^+$ (m/z = 344, 45%) and the dimer formed in the electrospray ($Na[Cu(salpn)]_2^+$, m/z = 709, 100%). The conductivity measurements confirmed that $[Cu(phen)_2]^{2+}$ and $[Cu(py_2pn)]^{2+}$ behave as 2 : 1 electrolytes, while [Cu(salpn)] is a non-electrolyte, in protic and non-protic solvents. The conductivity of $[Cu(phen)(OAc)_2]$ depends on the solvent. In protic solvents dissociation of one acetate takes place, as evidenced by the molar conductivity of 75 Ω cm^2 mol^{-1} in methanol which indicates the monocation $[Cu(phen)(OAc)(MeOH)]^+$ is the major species in this solvent, whereas in non-protic ones $[Cu(phen)(OAc)_2]$ behaves as a non-electrolyte.

The low temperature EPR spectra of solution of the four complexes in non-protic solvents (Fig. 2(a)) exhibit the characteristic pattern of Cu(II) with axial symmetry and a $d_{x^2-y^2}$ ground state, with $g_\parallel > g_\perp > 2.0023$ and the parallel component of the g tensor split into four lines through hyperfine coupling with the Cu(II) nuclear spin (I = 3/2), giving spectral parameters listed in Table 1. The g and A values enable to characterize the geometry of these complexes in solution. For tetragonal copper(II) complexes, an increase in the tetrahedral distortion from the square-planar geometry is reflected in the increase of g and the decrease of A values.[55] Usually, for Cu(II) complexes, the empirical f-factor ($g_\parallel/A_\parallel$) provides information on the tetrahedral distortion degree from the planar arrangement of the ligand, where the higher $g_\parallel/A_\parallel$ ratio implies a higher tetrahedral distortion. This factor is in the range of 105–135 cm^{-1} for complexes with the ligand close to planar

Table 1 EPR parameters of frozen DMF solutions of Cu(II) complexes

Compound	$A_{\parallel}/10^{-4}$ cm^{-1}	$g_{\parallel}$	$g_{\perp}$	$a_{N\perp}/10^{-4}$ cm^{-1}	$g_{\parallel}/A_{\parallel}$ (cm)
$[Cu(phen)_2(solv)]^{2+}$	158	2.29	2.07	—	145
$[Cu(phen)(CH_3CO_2)_2]$	173	2.29	2.07	13	132
$[Cu(Py_2pn)(solv)]^{2+}$	185	2.25	2.06	12	122
[Cu(salpn)]	190	2.23	2.05	14	117

disposition,[56] higher values imply a greater degree of distortion of the dihedral angles in the equatorial plane,[57] while complexes with tetrahedral geometry show f-factors > 180 cm^{-1}.[58] In the present case, the degree of tetrahedral distortion increases [Cu(salpn)] < $[Cu(py_2pn)]^{2+}$ < $[Cu(phen)(CH_3CO_2)_2]$ < $[Cu(phen)_2]^{2+}$. In line with this, five superhyperfine (shf) lines are observed on the $g_{\perp}$ component of [Cu(salpn)], $[Cu(py_2pn)]^{2+}$ and $[Cu(phen)(CH_3CO_2)_2]$, due to the coupling of the electronic spin with two ^{14}N (I = 1) nucleus[59] of the ligand disposed closer to the equatorial plane.

Paramagnetic ^1H NMR spectra of these complexes (Fig. 2(b)) are characterized by significant broadening and chemical shift displacement from the values observed for the ligands, without traces of the free ligands, indicating these compounds are stable towards metal dissociation. In the case of [Cu(salpn)] and $[Cu(py_2pn)]^{2+}$, the resonances of the aromatic ring and imino protons broaden and shift as a result of the paramagnetic relaxation induced by the Cu(II) ion, and the isotropic shift of the aromatic protons depends on the distance to the metal centre. For [Cu(salpn)] the broad signal at 33 ppm (ω = 3000 Hz) can be attributed to the imino protons, while signals at 8.9 (ω = 120 Hz), 6.9 (ω = 32 Hz) and −9.3 ppm (ω = 1480 Hz) can be assigned to H3(H3′), H4(H4′)/H5(H5′) and H6(H6′), respectively, on the basis of comparison with reported spectra for related Cu(II) complexes.[60,61] The protons belonging to both aromatic rings are indistinguishable because of their large relaxation rate values, so that the small distortions from the square planar geometry cannot be resolved. In the case of $[Cu(py_2pn)]^{2+}$, the pyridine ring proton resonances appear at 41 ($\omega \approx$ 4280 Hz), 11 (ω = 144 Hz) and 8.3 ppm (ω = 40 Hz), attributable to H2(H2′), H3/H4(H3′/H4′) and H5(H5′), respectively.[62] Also in this case, the deviation of the ligand from planarity is not large enough to distinguish the protons belonging to both pyridine rings. The ^1H NMR spectra of complexes $[Cu(phen)_2]^{2+}$ and $[Cu(phen)(OAc)_2]$ are characterized by broad peaks shifted down-field relative to the free ligands.[48] The spectrum of $[Cu(phen)_2]^{2+}$ consists of six signals in the region of 10 to 50 ppm, one set of three more intense resonances at 14 (ω = 96 Hz), 16 (ω = 208 Hz), and 20 (ω = 264 Hz) ppm, and another set of broader signals at 25 (ω = 890 Hz), 30 (ω = 580 Hz) and 41 (ω = 1650 Hz) ppm, belonging to non-equivalent protons of the two phen ligands, concurring with the more distorted geometry evidenced from EPR spectra. For $[Cu(phen)(OAc)_2]$, three intense peaks are observed at 13 (ω = 120 Hz), 17 (ω = 840 Hz) and 24 (ω = 560 Hz) ppm, attributable to H3/H8, H5/H6 and H4/H7 of phen, respectively, and one additional very broad signal at 38 ppm (ω = 1200 Hz) compatible with the methyl acetate shifted down-field in agreement with previously reported data for acetate bound to copper(II) ion.[63]

The electronic spectra of these compounds exhibit strong absorptions in the UV region where π–π* and ligand-to-metal charge transfer (LMCT) transition overlap except for the pπ-phenolate to dπ-Cu LMCT band of [Cu(salpn)] that shifts to longer wavelengths (at 366 nm). The four compounds possess coordination sites that can be occupied by solvent molecules affording pentacoordinated Cu(II) complexes. In particular, $[Cu(phen)_2]^{2+}$ shows a shift of the d–d transitions toward longer wavelengths relative to the other three complexes in acetonitrile solution (Fig. 3(a)). This broad band at ≈830 nm is consistent with a distortion towards the trigonal bipyramidal stereochemistry of the $[Cu(phen)_2(MeCN)]^{2+}$, while $[Cu(phen)(OAc)_2]$ shows a band at 706 nm indicating a tetrahedrally distorted square-planar geometry. $[Cu(py_2pn)(MeCN)]^{2+}$-which adopts a dome-shaped geometry with a weakly coordinated solvent molecule placed at the top of the pyramid-presents d–d transitions at 645 nm, and [Cu(salpn)] with a near square plane geometry, presents an absorption band at 608 nm.[64,65]

The redox potential of the complexes is another important indicator of the ability of the supporting ligand to control the reactivity of the metal centre to activate the peroxide. The cyclic voltammograms of the complexes are shown in Fig. 3(b) and S6–S9, and $E_{1/2}$ values are summarized in Table 2. For the two complexes with the Cu(II) ion bound to the N_4-donor set, the Cu(II)/Cu(I) redox potentials are less negative than for the two complexes with N_2O_2 first-coordination sphere. In particular, a large stabilization of the Cu(II) oxidation state is observed for [Cu(salpn)], in which the Cu(II) ion is closer to the plane of the ligand, while higher distortions around the metal centre in $[Cu(phen)_2]^{2+}$ stabilize the reduced Cu(I) compared to $[Cu(py_2pn)]^{2+}$.

Phenol oxidation

The redox potential, the total charge and the presence of coordinated labile solvent molecules favouring ligand exchange

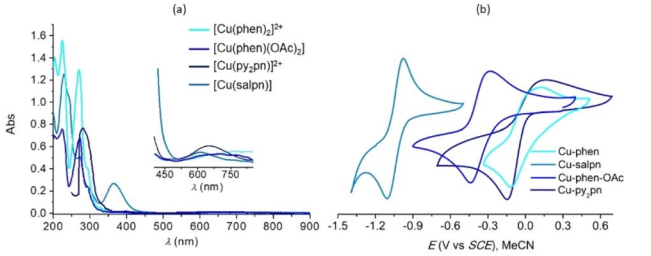

Fig. 3 (a) Electronic spectra of the Cu(II) complexes in MeCN. Inset: d–d transitions. (b) Cyclic voltammograms of the Cu(II) complexes in MeCN. [complex] = 1 mM, 0.1 M $TBAPF_6$ under argon, working electrode: glassy carbon, scan rate: 100 mV s^{-1}, T = 25 °C.

Table 2 Screening of Cu and Mn complexes as catalysts for phenol oxidation at pH 7 and 9, at 25 °C[a]

Entry	Catalyst	E (*vs.* SCE), mV	TONs pH 7	TONs pH 9
1	$[Cu(Py_2pn)]^{2+}$	−41 (MeCN)	6.9	7.7
2	$[Cu(phen)(CH_3CO_2)_2]$	−360 (MeCN)	6.5	7.5
3	$[Cu(phen)_2]^{2+}$	+2 (MeCN)	3.3	9.6
4	[Cu(salpn)]	−1003 (MeCN)	2.3	0.81
5	$[Mn(Py_2pn)]^{2+}$	>1000 (DMF)	5.1	3.1
6	$[Mn(3,5\text{-}Cl_2salpn)]^{+}$	+71 (DMF)	3.0	1.0
7	$[Mn(salpn)]^{+}$	−153 (DMF)	2.9	0.82
8	$[Mn(salpn)(\mu\text{-}O)]_2$	−507 (DCM)[70,71]	0.44[b]	0.67
9	$[Mn(3,5\text{-}Cl_2salpn)(\mu\text{-}O)]_2$	−235 (DCM)[70,71]	0.46[b]	0.81

[a] Conditions: [catalyst] = 2.7 μM, [phenol] = 0.27 mM, [4-AAP] = 0.68 mM, $[H_2O_2]$ = 3.3 mM. TON = mol of product per mol of catalyst. t = 2 h. Solvent: 1 : 5 MeCN(or DMF) : buffer phosphate of pH 7, 1 : 5 DMF : buffer borate of pH 9. [b] TONs achieved after 5 min.

with peroxide are features that can control the reactivity of the metal centre for catalysing phenol oxidation. Therefore, the ability of the above described four Cu(II) complexes to catalyse the oxidation of phenol by H_2O_2 was evaluated and compared to that of mononuclear Mn(II/III) and di-μ-oxo-Mn(IV) complexes, under the same reaction conditions. Kinetics studies were done in the presence of 4-AAP at pH 7 and 9, and TONs after 2 h of reaction, at 25 °C, are presented in Table 2. The di-μ-oxo-Mn(IV) dimers, which are good catalysts for H_2O_2 disproportionation,[66–69] showed the poorest catalytic performance at both pH. At pH 7, these dimers show activity during the first 5 min and then the phenol oxidation stops as most of the H_2O_2 decomposed. In general terms, the Cu and Mn complexes formed with py_2pn and phen are clearly better than those formed with salpn and Cl_2salpn ligands, at both pH. While $[Cu(phen)_2]^{2+}$ is a better catalyst than $[Cu(py_2pn)]^{2+}$ at pH 9, the last shows better activity than the Mn(II) analogue, and is twice as active as $[Cu(phen)_2]^{2+}$ at neutral pH, placing this complex as the best catalyst of this series of compounds for phenol oxidation under mild conditions. From redox potentials and TONs listed in Table 2, it is evident that the catalytic activity not only depends on the redox potential, but that the combination of a suitable redox potential, 2+ total charge and an axially coordinated solvent molecule favour peroxide activation by $[Cu(py_2pn)]^{2+}$.

Kinetic studies of phenol oxidation by H_2O_2 catalysed by $[Cu(py_2pn)]^{2+}$

$[Cu(py_2pn)]^{2+}$ shows a clear catalytic effect on the phenol oxidation by H_2O_2 at 25 °C, either at pH 7 and 9, far exceeding the conversion achieved under the same conditions in the absence of the catalyst.

When the catalysed reaction was performed at 50 °C, keeping constant the other conditions employed in the screening study, a remarkable increase of turnover frequency (TOF) values was observed, from $TOF_{pH7}^{25} = 3.45\ h^{-1}$ to $TOF_{pH7}^{50} = 57\ h^{-1}$ and from $TOF_{pH9}^{25} = 3.85\ h^{-1}$ to $TOF_{pH9}^{50} = 80\ h^{-1}$, placing this complex among the most active Cu(II) catalysts reported for

Table 3 Comparative conversions in catalyzed phenol oxidation by H_2O_2

Catalyst	Reaction conditions	TOF (h^{-1})	Ref.
$[Cu(py_2pn)]^{2+}$	pH 7, 50 °C	56	This work
	pH 9, 50 °C	80	
CuL^1Cl_2	pH 11.6, 80 °C	109	14
CuL^2	H_2O, 70 °C	76	15
$CuL^3(OEt)$	MeCN, reflux	61	16
CuL^1Cl_2	pH 11.6, 65 °C	57	14
CuL^{4a}	H_2O, 65 °C	35	17
CuL^5	H_2O, 80 °C	31	18
CuL^6	H_2O, 80 °C	21	18
$CuL^7{}_2$	pH 3, 110 °C	13.7	19
$CuL^8{}_2$	pH 5, 110 °C	12	20
$CuL^9{}_2$	MeCN, microwave (280 W)	10.3	21
CuL^{10a}	H_2O, 65 °C	7.0	17
CuL^{6a}	H_2O, 65 °C	4.2	17
CuL^2	MeCN, 80 °C	0.3	25

[a] Complex generated *in situ*. L^1 = 5,7,12,14-tetramethyldibenzo[*b*,*i*]-1,4,8,11-tetraazacyclotetradecane, HL^2 = *N*,*N*-bis(salicylidene) diethylenetriamine, HL^3 = methyl-2-(2-hydroxybenzylideneamino)-4,5,6,7-tetrahydrobenzo[*b*]-thiophene-3-carboxylate, L^4 = *N*,*N*′-bis(2-pyridinylmethylen)butane-1,4-diamine, H_2L^5 = 1,2-bis(5-chlorosalicylidene)ethylenediamine, H_2L^6 = 1,2-bis(salicylidene) ethylenediamine, HL^7 = propyl-(1H-pyrrol-2-ylmethylene)imine, HL^8 = *N*-phenylsalicylaldimine derivatives, HL^9 = picolinate, H_2L^{10} = 1,4-bis(salicylidene)butanediamine. TOF = mol of product per mol of catalyst per hour.

phenol oxidation, as shown in Table 3. Given the impressive increase in the oxidation rate with temperature, the reaction kinetic was evaluated at 25 and 50 °C by monitoring the formation of *p*-quinoneimide (*p*-QI) at 500 nm, in the presence of 4-AAP. In all the kinetic runs, the [4-AAP] was kept constant, and the $[catalyst]_0$, $[phenol]_0$ and $[H_2O_2]_0$ were varied in the ranges 0.16–53 μM, 0.05–4.0 mM and 0.17–17 mM, respectively. In each case, the initial rate (r_0) of *p*-QI formation was determined from the Abs^{500} *vs.* t curve affording the values listed in Tables S3–S6.

The dependence of r_0 on the $[catalyst]_0$, $[phenol]_0$ and $[H_2O_2]_0$ at pH 7 and 9 is shown in Fig. 4. While r_0 shows saturation with $[catalyst]_0$ and $[phenol]_0$, the dependence of r_0 on $[H_2O_2]$ is more complex, as can best be observed at pH 9 where r_0 grows, goes through a maximum and then decreases as $[H_2O_2]_0$ increases. The whole set of experimental data at each temperature and pH could be fitted to eqn (1),† and the values for the kinetic parameters that best describe the data are listed in Table 4. Curves simulated with the parameters obtained from the fit of the experimental data to eqn (1) (solid lines in Fig. 4) show the goodness of fit to the experimental values.

$$r_0^{QI} = \frac{A[phOH][H_2O_2][catalyst]}{B + C[phOH] + D[catalyst] + [phOH][H_2O_2]^2} \quad (1)$$

† At pH 7, a correction was applied on eqn (1) by adding a second term with a very minor contribution, only dependent on [phOH], which corresponds to the uncatalyzed oxidation of phenol by the dissolved O_2.

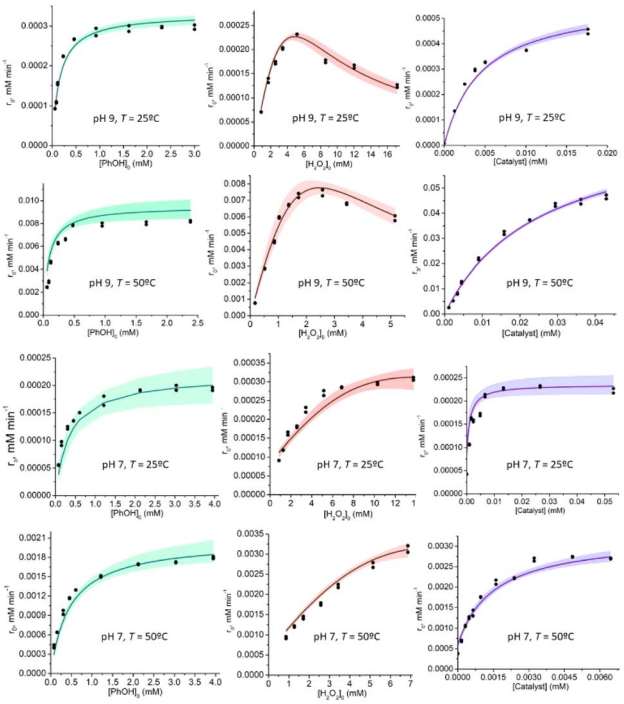

Fig. 4 Experimental (dots) and calculated (solid line) initial rate values (r_0) for the formation of *p*-QI, at different pH, *T* and reactants concentrations. 95% confidence bands are shown.

The rate law can be interpreted through the mechanism in the Scheme 1. The first step of this mechanism consists in the formation of the $[Cu(py_2pn)OOH]^+$ adduct. The fast formation of the Cu(II)-hydroperoxide species in mixtures of $[Cu(py_2pn)]^{2+}$ and H_2O_2 of different ratios has been previously reported, and the adduct characterized by different spectroscopies and DFT calculations.[27] $[Cu(py_2pn)OOH]^+$ then can (i) oxidize phenol to yield *p*-QI in the presence of 4-AAP, (ii) react with a second complex to form the *trans*-1,2-peroxodicopper(II) dimer,[27] which is known to decompose to yield O_2 and the reduced form of the catalyst, or (iii) give rise to products different from *p*-QI, through three competitive paths.

In this mechanism, the $[Cu(py_2pn)OOH]^+$ adduct is the proposed oxidant, an intermediate that has also been proposed

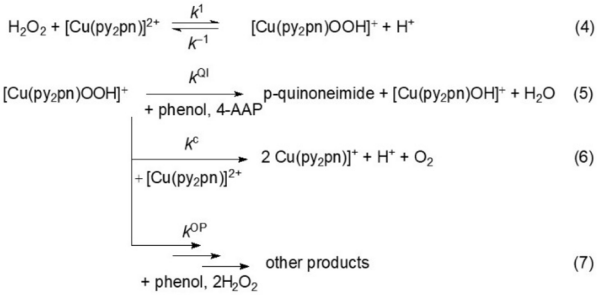

Scheme 1 Mechanism for the H_2O_2 oxidation of phenol catalysed by $[Cu(py_2pn)]^{2+}$.

in aryl hydroxylation and oxidative *N*-dealkylation reactions catalyzed by Cu(II) complexes.[72–75] Assuming that the intermediate $[Cu(py_2pn)OOH]^+$ is in steady state, eqn (2) can be derived from the mechanism in Scheme 1 for the rate of formation of *p*-QI, which is analogous to the experimental rate law (1).

$$v^{QI} = \frac{k^1 k^{QI}[phOH][H_2O_2][catalyst]}{k^{-1} + k^{QI}[phOH] + k^c[catalyst] + k^{OP}[phOH][H_2O_2]^2} \quad (2)$$

Based on this mechanism, $A = k^{QI}\,k^1/k^{OP}$, $B = k^{-1}/k^{OP}$, $C = k^{QI}/k^{OP}$, and $D = k^C/k^{OP}$. Therefore, A/C affords k^1, the rate constant for the formation of the $[Cu(py_2pn)OOH]^+$ adduct, which experiences a large increase with increasing temperature. The activation energy values associated with k^1 at both pH values, $E_a^{pH7} = 21 \mp 4$ kcal mol^{-1} and $E_a^{pH9} = 35 \mp 4$ kcal mol^{-1} explains the slow formation of the adduct at the lower temperature in basic medium. From the values of parameters listed in Table 4, the minimum [phenol]/[catalyst] ratio that favours the formation of *p*-QI over the catalase reaction can be calculated through the r^{QI}/r^C ratio in eqn (3).

$$\frac{r^{QI}}{r^C} = \frac{k^{QI}[phenol]}{k^C[catalyst]} \quad (3)$$

Therefore, at pH = 7, $r^{QI} > r^C$ when [phenol]/[catalyst] > 260, while at pH = 9, $r^{QI} > r^C$ when [phenol]/[catalyst] > 120. For this reason, the catalyst proportion must be kept below 0.4 mol%, to

Table 4 Kinetic parameters for the H_2O_2 oxidation of phenol catalysed by $[Cu(py_2pn)]^{2+}$

	pH 7		pH 9	
	25 °C	50 °C	25 °C	50 °C
$A = k^{QI}\,k^1/k^{OP}$ (mM min^{-1})	2.2 ± 0.3	(1.9 ± 0.3) × 10	0.85 ± 0.05	14.2 ± 0.9
$B = k^{-1}/k^{OP}$ (mM^3)	—	—	—	0.7 ± 0.2[a]
$C = k^{QI}/k^{OP}$ (mM^2)	(0.5 ± 0.2) × 10^2	(2.6 ± 0.8) × 10	11 ± 1	2 ± 1
$D = k^C/k^{OP}$ (mM^2)	(1.3 ± 0.2) × 10^4	(0.6 ± 0.1) × 10^4	(13.1 ± 0.8) × 10^2	(1.6 ± 0.1) × 10^2
$A/C = k^1$ (mM^{-1} min^{-1})	0.04 ± 0.02	0.7 ± 0.2	0.08 ± 0.01	7 ± 4
$k^{CAT} = k^C\,k^1$ (mM^{-2} min^{-1})		(1.0 ± 0.1) × 10^{-1}		(3.2 ± 0.5) × 10^{-1}
$k^{QI\text{-}f} = k^{QI}\,k^1$ (mM^{-2} min^{-1})		(0.4 ± 0.2) × 10^{-3}		(0.4 ± 0.2) × 10^{-2}
$k^{OP\text{-}f} = k^{OP}\,k^1$ (mM^{-4} min^{-1})		(1.6 ± 0.7) × 10^{-5}		(0.2 ± 0.1) × 10^{-2}

[a] Parameter *B* is significant only at pH 9 and 50 °C, under the other conditions it is negligible.

prevent the catalase reaction from being favoured at any pH. Besides, the values of parameter C (k^{QI}/k^{OP}) indicate that the formation of *p*-QI is favoured over the oxidation products not trapped by 4-AAP at both pH, although the last increases with increasing pH and temperature. Furthermore, given the higher order dependence of r^{OP} on $[H_2O_2]$, this path is favoured at high $[H_2O_2]$ where trapping by 4-AAP is less effective. This becomes particularly evident at pH 9 and 50 °C (Fig. 4), where the r^{OP} path strongly competes with *p*-QI formation at high $[H_2O_2]$. The kinetics of the catalysed H_2O_2 dismutation (r^{CAT}) was independently evaluated at both pH and 50 °C, affording the third order rate law $r_0^{CAT} = k^{CAT}[\text{catalyst}]^2[H_2O_2]$, with k^{CAT} values given in Table 4. Knowing the values of k^{CAT} ($k^{CAT} = k^C k^1$, $mM^{-2}\ min^{-1}$), the third order rate constants for the formation of *p*-QI, ($k^{QI\text{-}f} = k^{QI} k^1$, $mM^{-2}\ min^{-1}$) and the rate constants for the path leading to other oxidation products ($k^{OP\text{-}f} = k^{OP} k^1$, $mM^{-4}\ min^{-1}$) were estimated at pH 9 (Table 4). The higher rates observed in basic medium for phenol oxidation are related, in part, to the lower oxidation potential of phenol at the higher pH,[76] and the increase of k^1 value.

As it is known, the oxidative coupling of phenol with 4-AAP quantitatively produces *p*-QI as the only product.[77–79] Therefore, the selectivity of phenol oxidation catalysed by $[Cu(py_2pn)]^{2+}$ was examined by HPLC analysis at pH 9 in the absence of 4-AAP. At 25 °C, the catalyst mainly promoted the formation of hydroquinone, whereas catechol was not detected. This preference for *para*-hydroxylation of phenol has previously been observed for other Cu-based catalysts at low temperature,[13,22,80,81] and differs from that of related catalysts tested at T > 60 °C.[14–21,25] Even when catechol was not detected, its formation cannot be excluded, as catechol is oxidized faster than phenol, affording $TOF_{pH9}{}^{25} = 25\ h^{-1}$ *vs.* 3.85 h^{-1} found for phenol, a difference that may result from the lower oxidation potential of catechol compared to phenol.[76] However, the catalysed oxidation of catechol yielded 1,2,4-trihydroxybenzene as the main product, a compound not detected during oxidation of phenol at 25 °C. At 50 °C, the *p:o* selectivity decreased to 70:30, as well as *p*-benzoquinone formed as byproduct, as a consequence of the overoxidation of hydroquinone. The results suggest that the initial phenol oxidation catalysed by $[Cu(py_2pn)]^{2+}$ strongly depends on temperature, occurring predominantly at the *para*-position at the lower temperature used here. The observed regioselectivity can be explained by considering that the oxidation starts with the binding of phenol to the copper centre of $[(py_2pn)CuOOH]^+$, and that a concerted proton/electron transfer generates a phenoxyl radical that remains within the metal coordination sphere, so that subsequent hydroxylation occurs at the less hindered and electronically favoured *p*-position. As the temperature increases, the phenoxyl radical moves faster away from the metal centre, and both *o*/*p* positions become available to react with a second $[(py_2pn)CuOOH]^+$ in a fast step.

Immobilization of catalysts

Taking into account that the catalytic performance of a complex can be improved by supporting it on a solid matrix,[82,83] while incorporation of the complex into the channels of a mesoporous material allows for isolation, confinement and protection towards hydrolysis,[84] complexes $[Cu(py_2pn)]^{2+}$ and $[Cu(phen)_2]^{2+}$ were encapsulated into mesoporous SBA-15 silica with the intention of testing the effect of immobilization on the catalysis of phenol oxidation by H_2O_2. Insertion of these two complexes into the mesoporous matrix of SBA-15 silica was performed through the exchange of silanol protons of the silica surface by the cationic complexes, yielding Cu-py_2pn@SBA-15 and Cu-phen@SBA-15 hybrids. The textural properties of SBA-15, Cu-py_2pn@SBA-15 and Cu-phen@SBA-15, were analysed by nitrogen adsorption–desorption measurements at 77 K (Fig. 5(a)). The three samples exhibit type IV isotherms with a sharp rise at relative pressure p/p_0 = 0.65–0.75, typical of mesoporous materials with one-dimensional cylindrical channels. The sharpness of the jump is characteristic of materials with a uniform mesopore size distribution. The similarity of the isotherms of neat silica to those of both hybrid materials suggests that the structural features of SBA-15 are preserved after the catalyst immobilization, except for the slight decrease in the total volume of adsorbed N_2 (both curves are shifted downward relative to that of pure silica) consistent with the insertion of the complexes in the mesoporous matrix. This is also evident in Table 5, where it can be observed that the uptake of the catalyst reduces the BET surface area, total pore volume and pore diameter.

The TEM images confirms that the highly ordered mesostructure of SBA-15 is retained in the hybrid materials, all exhibiting a regular array of parallel cylindrical channels (Fig. 6(a)–(c)). These mesoporous materials display open porosity, with the pore network exposed at the particles surface, a feature suitable for the substrate to interact with the catalyst. Statistical analysis of the TEM images afforded average pore diameter of 3.1 ± 0.8 nm and 4.3 ± 0.8 nm, and wall thickness of 4.1 ± 0.9 nm and 3.8 ± 0.6 nm, for Cu-py_2pn@SBA-15 and Cu-phen@SBA-15, respectively. The thick walls confer robustness to the catalytic material and pore diameter values are in the range of those calculated from the sorption isotherms, confirming the synthesized silica is appropriate to house the complexes which are around 1.2 nm width (calculated from crystal structures).

EPR spectroscopy was used to examine if the geometry around the metal centre is modified by the inclusion of the complex within the silica pore. The low-temperature X-band

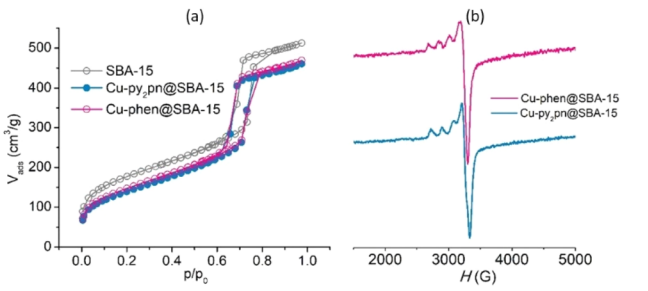

Fig. 5 (a) Adsorption–desorption N_2 isotherms of SBA-15 and hybrid materials. (b) X-band EPR spectra of hybrids, at 100 K.

Table 5 Textural characterization of mesoporous materials[a]

	S_{BET} ($m^2\ g^{-1}$)	$V_{\mu P}$ ($cm^3\ g^{-1}$)	V_{MP} ($cm^3\ g^{-1}$)	V_{TP} ($cm^3\ g^{-1}$)	w_P (nm)	mmol complex/100 g material
SBA-15	641	0.03	0.64	0.79	4.9	—
Cu-phen@SBA-15	530	—	0.60	0.72	4.4	1.3
Cu-py_2bn@SBA-15	501	—	0.57	0.71	4.4	3.4

[a] $V_{TP} = V_{\mu P} + V_{primary\ MP} + V_{secondary\ MP}$, MP = mesopore; μP = micropore; w_p = pore diameter.

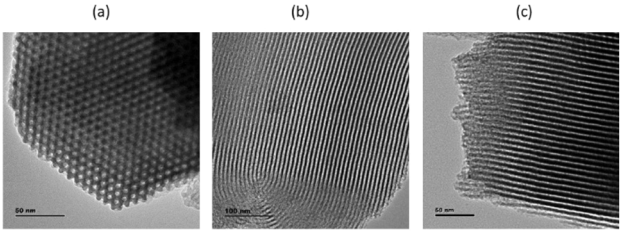

Fig. 6 TEM images of (a) SBA-15, (b) Cu-phen@SBA-15 and (c) Cu-py_2pn@SBA-15.

EPR spectra of Cu-py_2pn@SBA-15 and Cu-phen@SBA-15 are shown in Fig. 5(b). Upon encapsulation, the paramagnetic centre of the complex is diluted in the mesoporous matrix giving a well-defined axial EPR signal, with spectral parameters $g_{\|} = 2.227$, $g_{\perp} = 2.047$ and $A_{\|} = 183 \times 10^{-4}\ cm^{-1}$ for Cu-py_2pn@SBA-15, and $g_{\|} = 2.273$, $g_{\perp} = 2.061$ and $A_{\|} = 173 \times 10^{-4}\ cm^{-1}$ for Cu-phen@SBA-15. Moreover, the f-factor $(g_{\|}/A_{\|}) = 122$ and 131 cm, suggest that in Cu-py_2pn@SBA-15 the Cu(II) ion retains the slightly distorted tetragonal coordination geometry of the complex in solution, while insertion of $[Cu(phen)_2]^{2+}$ into the pores leads to a tetragonal geometry around the copper centre much less distorted than in solution.

Phenol oxidation catalysed by the immobilized catalysts

The ability of Cu-py_2pn@SBA-15 and Cu-phen@SBA-15 to catalyse phenol oxidation by H_2O_2 was evaluated, at pH 9 and 25 °C, employing the reagents in the same proportion as used in the screening essays in homogeneous media, except that 4-AAP was not added to the reaction mixture. Before testing the hybrid materials as catalysts, their stability in the reaction medium was verified by UV-vis spectroscopy. The solids were suspended in buffer of pH 9, at room temperature, sonicated and then centrifuged before the spectrophotometric measurements. In both cases, the release of the complexes was negligible, as confirmed by ICP analysis of the supernatant. The reactivity of the heterogeneous catalysts, expressed in terms of TON (Table 6) after 2 h of reaction, highlights the positive impact of confinement. Besides, isolation of the catalyst in the silica matrix avoids the formation of the peroxo-diCu dimer involved in H_2O_2 disproportionation, thus decreasing this competitive reaction. Therefore, for both complexes, higher conversions were reached with the encapsulated catalyst compared to the homogenous analogue. In the case of Cu-py_2pn@SBA-15, the interaction of the metal centre with the pore surface boosts the reaction rate with slight change of the ligand conformation. Instead the pore forces Cu-phen@SBA-15 to adopt a constrained and more reactive conformation, probably with the two phen ligands nearer the equatorial plane of the Cu(II) ion, as evidenced by EPR spectroscopy, resulting in a greater improvement of the catalytic performance than for Cu-py_2pn@SBA-15.

Table 6 Heterogeneous catalyzed oxidation of phenol by H_2O_2[a]

Catalyst	$g_{\|}/A_{\|}$ (cm)	TON
$[Cu(py_2pn)]^{2+}$	122	7.7
Cu-py_2pn@SBA-15	122	14
$[Cu(phen)_2]^{2+}$	145	9.6
Cu-phen@SBA-15	131	24

[a] Conditions: [catalyst] = 2.7 μM, [phenol] = 0.27 mM, $[H_2O_2]$ = 3.3 mM. TON = mol of product per mol of catalyst. t = 2 h. Solvent: 1 : 5 DMF : buffer borate of pH 9. T = 25 °C.

Conclusions

Among the complexes evaluated in this work, $[Cu(py_2pn)]^{2+}$ proved to be a good catalyst for phenol oxidation by H_2O_2 achieving good conversions at low temperature, comparable or better than those reported for related Cu(II) catalysts at higher temperature. The total charge, geometry, redox potential and a labile solvent molecule at the axial position impact the $[Cu(py_2pn)]^{2+}$ performance. Its catalytic activity strongly depends on pH and temperature, essentially due to the increase of the rate of formation of the catalyst-hydroperoxide adduct with pH and temperature. At 50 °C and pH 9, phenol conversion is favoured but selectivity is low, while at 25 °C phenol is preferentially oxidized to hydroquinone. Catalase activity, that occurs through a peroxo-diCu dimer, competes with phenol oxidation at high catalyst concentration, while overoxidation reactions become important at high pH and temperature. Immobilization of the catalyst on mesoporous silica takes place with retention of the complex geometry within the pores and causes a considerable improvement in activity. Incorporation of $[Cu(phen)_2]^{2+}$-the other complex exhibiting high activity at pH 9 and room temperature-into mesoporous silica forces the metal centre to adopt a more constrained geometry leading to an even higher enhancement of activity with respect to the homogeneous complex. Therefore, encapsulation of the cationic Cu(II) complexes into SBA-15 silica is a suitable approach to catalyse the oxidation of phenol by H_2O_2 at room temperature.

Conflicts of interest

There are no conflicts to declare.

Data availability

CCDC 2495739 ($[Cu(phen)_2(MeCN)](ClO_4)_2$), 2495740 ($[Cu(phen)_2Cl]ClO_4$) and 2495857 ($[\{Cu(phen)(OAc)_2\}_2$-$\mu$-$H_2O]$) contain the supplementary crystallographic data for this paper.[85a–c]

The data supporting this article have been included as part of the supplementary information (SI). Supplementary information: synthesis, elemental analysis, crystal structures, mass spectra and cyclic voltammograms of complexes; Tables of initial rates. See DOI: https://doi.org/10.1039/d5ra08195e.

Acknowledgements

This work was supported by the National University of Rosario (PID UNR 80020220700136UR), Consejo Nacional de Investigaciones Científicas y Técnicas (CONICET, PIP 0852 and PUE 0068), Agencia Nacional de Promoción Científica y Tecnológica (ANPCyT, PICT-2019-03276), and Agencia Santafecina de Ciencia, Tecnología e Innovación (ASaCTEI, PEICID-2023-214). We thank Juan Carlos González for HPLC measurements. The Bruker D8 QUEST ECO Photon II CPAD Diffractometer was purchased with funds from ANPCyT (PME 2015-0022) and CONICET.

Notes and references

1 L. Krumenacker, M. Costantini, P. Pontal and J. Sentenac, In *Kirk-Othmer Encyclopedia of Chemical Technology*, Wiley, Hoboken, NJ, USA, 2000.
2 E. Naranov, D. Ramazanov, M. Agliullin, O. Sinyashin and A. Maximov, *Catalysts*, 2024, **14**, 930.
3 G. Centi and S. Perathoner, *Catal. Today*, 2009, **143**, 145–150.
4 M. R. Mäkelä, E. L. Bredeweg, J. K. Magnuson, S. E. Baker, R. P. de Vries and K. Hildén, *Microbiol. Spectr.*, 2016, **4**, DOI: 10.1128/microbiolspec.FUNK-0017-2016.
5 Y. Sugano, T. Yoshida and R. Fernandez-Lafuente, *Int. J. Mol. Sci.*, 2021, **22**, 5556.
6 S. Valimets, L. Schwaiger, A. Bennett, D. Maresch, R. Ludwig, S. Hann, D. Linde, F. J. Ruiz-Dueñas and C. Peterbauer, *ACS Omega*, 2024, **9**, 45025–45034.
7 I. Ivanović-Burmazović and R. van Eldik, *Dalton Trans.*, 2008, 5259–5275.
8 A. D. Bokare and W. J. Choi, *Hazard Mater.*, 2014, **275**, 121–135.
9 L. T. Nguyen, W. F. Ho and K.-L. Yang, *RSC Adv.*, 2020, **10**, 17408–17415.
10 M. Šebela, G. Zoppellaro and Z. Trávníček, *J. Inorg. Biochem.*, 2025, **268**, 112911.
11 M. Beltran-Torres, R. Sugich-Miranda, H. Santacruz-Ortega, L. Machi, M. Inoue, E. F. Velázquez-Contreras, Y. Soberanes, H. Höpfl, R. Pérez-González, R. E. Navarro, A. J. Salazar-Medina and R. R. Sotelo Mundo, *ACS Omega*, 2019, **4**, 22487–22496.
12 Z. Zhang, G. Yin and B. Andrioletti, *Transit. Met.Chem.*, 2022, **47**, 189–211.
13 Q.-Q. Hu, Q.-F. Chen, H.-T. Zhang, J. -Yi Chen, R.-Z. Liao and M.-T. Zhang, *Dalton Trans.*, 2025, **54**, 1896–1904.
14 V. K. Bansal, R. Kumar, R. Prasad, S. Prasad and Niraj, *J. Mol. Catal. A:Chem*, 2008, **284**, 69–76.
15 M. R. Maurya and S. Sikarwar, *J. Mol. Catal. A:Chem*, 2007, **263**, 175–185.
16 A. Mobinikhaledi, M. Zendehdel and P. Safari, *Transit. Met. Chem.*, 2014, **39**, 431–442.
17 E. A. Karakhanov, A. L. Maximov, Y. S. Kardasheva, V. A. Skorkin, S. V. Kardashev, E. A. Ivanova, E. Lurie-Luke, J. A. Seeley and S. L. Cron, *Ind. Eng. Chem. Res.*, 2010, **49**, 4607–4613.
18 S. Deshpande, D. Srinivas and P. Ratnasamy, *J. Catal.*, 1999, **188**, 261–269.
19 J. N. Mugo, S. F. Mapolie and J. L. VanWyk, *Inorg. Chim. Acta*, 2010, **363**, 2643–2651.
20 J. L. van Wyk, S. Mapolie, A. Lennartson, M. Håkansson and S. Jagner, *Z. Naturforsch.*, 2007, **62b**, 331–338.
21 K. K. Bania and R. C. Deka, *J. Phys. Chem. C*, 2013, **117**, 11663–11678.
22 X.-G. Meng, J. Zhu, J. Yan, J.-Q. Xie, X.-M. Kou, X.-F. Kuang, L.-F. Yu and X.-C. Zeng, *J. Chem. Technol. Biotechnol.*, 2006, **81**, 2–7.
23 N. Nath, A. Routaray, Y. Das, T. Maharana and A. K. Sutar, *Kinet. Catal.*, 2015, **56**, 718–732.
24 K. Gupta and A. Sutar, *J. Mol. Catal. A:Chem*, 2008, **280**, 173–185.
25 M. R. Maurya, J. J. Titinchi and S. Chand, *J. Mol. Catal. A: Chem.*, 2003, **201**, 119–130.
26 M. Yamada, K. D. Karlin and S. Fukuzumi, *Chem. Sci.*, 2016, **7**, 2856–2863.
27 M. Richezzi, J. Ferreyra, J. Puzzolo, L. Milesi, C. M. Palopoli, D. M. Moreno, C. Hureau and S. R. Signorella, *Eur. J. Inorg. Chem.*, 2022, e202101042.
28 A. A. Schilt and R. C. Taylor, *J. Inorg. Nucl. Chem.*, 1959, **9**, 211–221.
29 M. Devereux, D. O'Shea, M. O'Connor, H. Grehan, G. Connor, M. McCann, G. Rosair, F. Lyng, A. Kellett, M. Walsh, D. Egan and B. Thati, *Polyhedron*, 2007, **26**, 4073–4084.
30 I. I. Ebralidze, G. Leitus, L. J. W. Shimon, Y. Wang, S. Shaik and R. Neumann, *Inorg. Chim. Acta*, 2009, **362**, 4713–4720.
31 M. R. Maurya, S. J. J. Titinchi and S. Chand, *Appl. Catal., A*, 2002, **228**, 177–187.
32 M. Richezzi, S. Signorella, C. Palopoli, N. Pellegri, C. Hureau and S. R. Signorella, *Inorganics*, 2023, **11**, 359.
33 C. Palopoli, J. Ferreyra, A. Conte-Daban, M. Richezzi, A. Foi, F. Doctorovich, E. Anxolabéhère-Mallart, C. Hureau and S. R. Signorella, *ACS Omega*, 2019, **4**, 48–57.
34 J. W. Gohdes and W. H. Armstrong, *Inorg. Chem.*, 1992, **31**, 368–373.
35 Bruker, *APEX4 v2022.10-1*, Bruker AXS Inc., Madison, WI, USA, 2022.
36 Bruker, *SAINT V8.40B*, Bruker AXS Inc., Madison, WI, USA, 2019.
37 G. M. Sheldrick, *Acta Cryst.*, 2015, **A71**, 3–8.
38 G. M. Sheldrick, *Acta Cryst.*, 2015, **C71**, 3–8.

39 ORTEP3 for Windows and L. J. J. Farrugia, *Appl. Crystallogr.*, 1997, **30**, 565.
40 G. B. Payne, P. H. Deming and P. H. Williams, *J. Org. Chem.*, 1961, **26**, 659–663.
41 J. Ferreyra and S. Signorella, Repository of Academic Data RDA-UNR/Experimental and kinetic data, 2025, DOI: 10.57715/UNR/NGWTC1.
42 R Core Team. *R: A Language and Environment for Statistical Computing*. R Foundation for Statistical Computing, Vienna, Austria, 2025, https://www.R-project.org/.
43 T. V. Elzhov, K. M. Mullen, A.-N. Spiess, B. Bolker, minpack.lm: R Interface to the Levenberg-Marquardt Nonlinear Least-Squares Algorithm Found in MINPACK, Plus Support for Bounds. *R Package Version 1.2-4*. R Foundation for Statistical Computing, Vienna, Austria, 2023, https://CRAN.R-project.org/package=minpack.lm.
44 K. Amournjarusiri and B. J. Hathaway, *Acta Cryst.*, 1991, **C47**, 1383–1385.
45 A. W. Addison, T. Nageswara Rao, J. Reedijk, J. van Rijn and G. C. Verschoor, *J. Chem. Soc. Dalton Trans.*, 1984, 1349–1356.
46 M.-D. Serb, B. Calmuschi-Cula, F. Dumitru, T. Dols, U. Englert and C. Guran, *Acta Cryst.*, 2007, **E63**, m1292–m1293.
47 D. Boys, C. Escobar and S. Martínez-Carrera, *Acta Cryst.*, 1981, **B37**, 351–355.
48 Y.-B. Wei and P. Yang, *Acta Cryst.*, 2004, **E60**, m429–m431.
49 A. Crispini, C. Cretu, D. Aparaschivei, A. A. Andelescu, V. Sasca, V. Badea, I. Aiello, E. I. Szerb and O. Costisor, *Inorg. Chim. Acta*, 2018, **470**, 342–351.
50 M. Barquín, M. J. González Garmendia, L. Larrínaga, E. Pinilla and M. R. Torres, *Z. Anorg. Allg. Chem.*, 2005, **631**, 2151–2155.
51 M. J. Andrews, A. Carpentier, A. M. Z. Slawin, D. B. Cordes, S. A. Macgregor and A. J. B. Watson, *ACS Catal.*, 2023, **13**, 11117–11126.
52 M. G. B. Drew, R. N. Prasad and R. P. Sharma, *Acta Cryst.*, 1985, **C41**, 1755–1758.
53 L. C. Nathan, J. E. Koehne, J. M. Gilmore, K. A. Hannibal, W. E. Dewhirst and T. D. Mai, *Polyhedron*, 2003, **22**, 887–894.
54 M. Hasegawa, K. Kumagai, M. Terauchi, A. Nakao, J. Okubo and T. Oshi, *Monatsh. Chem.*, 2022, **133**, 285–298.
55 C. M. Wansapura, C. Juyoung, J. L. Simpson, D. Szymanski, G. R. Eaton, S. S. Eaton and S. Fox, *J. Coord. Chem.*, 2003, **56**, 975–993.
56 U. Sakaguchi and A. W. Addison, *J. Chem. Soc., Dalton Trans.*, 1979, 600–608.
57 U. El-Ayaan and I. M. Gabr, *Spectrochim. Acta A*, 2007, **67**, 263–272.
58 P. J. Benites, D. S. Rawaty and J. M. Zaleski, *J. Am. Chem. Soc.*, 2000, **122**, 7208–7217.
59 E. Carter, E. L. Hazeland, D. M. Murphy and B. D. Ward, *Dalton Trans.*, 2013, **42**, 15088–15096.
60 M. Bühl, S. E. Ashbrook, D. M. Dawson, R. A. Doyle, P. Hrobárik, M. Kaupp and I. A. Smellie, *Chem. Eur. J.*, 2016, 15328–15339.
61 I. Bertini, A. Dei and A. Scozzafava, *Inorg. Chem.*, 1975, **14**, 1526–1528.
62 M. Brink, R. A. Rose and R. C. Holz, *Inorg. Chem.*, 1996, **35**, 2878–2885.
63 I. Y. Ahmed and A. L. Abu-Hijleh, *Inorg. Chim. Acta*, 1982, **61**, 241–246.
64 G. Murphy, C. O'Sullivan, B. Murphy and B. Hathaway, *Inorg. Chem.*, 1998, **37**, 240–248.
65 C. O'Sullivan, G. Murphy, B. Murphy and B. Hathaway, *J. Chem. Soc., Dalton Trans.*, 1999, 1835–1844.
66 E. J. Larson and V. L. Pecoraro, *J. Am. Chem. Soc.*, 1991, **113**, 3810–3818.
67 E. J. Larson and V. L. Pecoraro, *J. Am. Chem. Soc.*, 1991, **113**, 7809–7810.
68 S. Signorella, A. Rompel, K. Büldt-Karentzopoulos, B. Krebs, V. L. Pecoraro and J.-P. Tuchagues, *Inorg. Chem.*, 2007, **46**, 10864–10868.
69 C. Palopoli, G. Gómez, A. Foi, F. Doctorovich, S. Mallet-Ladeira, C. Hureau and S. Signorella, *J. Inorg. Biochem.*, 2017, **167**, 49–59.
70 M. J. Baldwin, T. L. Stemmler, J. Pamela, J. Riggs-Gelasco, M. L. Kirk, J. E. Penner-Hahn and V. L. Pecoraro, *J. Am. Chem. Soc.*, 1994, **116**, 11349–11356.
71 M. J. Baldwin, A. Gelasco and V. L. Pecoraro, *Photosynt. Res.*, 1993, **38**, 303–308.
72 A. K. Nath, A. Ghatak, A. Dey and S. G. Dey, *Chem. Sci.*, 2021, **12**, 1924–1929.
73 R. Trammell, K. Rajabimoghadam and I. Garcia-Bosch, *Chem. Rev.*, 2019, **119**, 2954–3031.
74 D. Maiti, H. R. Lucas, A. A. N. Sarjeant and K. D. Karlin, *J. Am. Chem. Soc.*, 2007, **129**, 6998–6999.
75 S. Kim, J. W. Ginsbach, J. Y. Lee, R. L. Peterson, J. J. Liu, M. A. Siegler, A. A. Sarjeant, E. L. Solomon and K. D. Karlin, *J. Am. Chem. Soc.*, 2015, **137**, 2867–2874.
76 P. Wardman, *J. Phys. Chem. Ref. Data*, 1989, **18**, 1637–1755.
77 E. Emerson, *J. Org. Chem.*, 1943, **8**, 417–428.
78 Y. Fiamegos, C. Stalikas and G. Pilidis, *Anal. Chim. Acta*, 2002, **467**, 105–114.
79 C. Z. Katsaounos, E. K. Paleologos, D. L. Giokas and M. I. Karayannis, *Intern. J. Environ. Anal. Chem.*, 2003, **83**, 507–514.
80 L.-G. Qiu, A. J. Xie and L.-D. Zhang, *Adv. Mater.*, 2005, **17**, 689–692.
81 Y. Wang, J. Guan, B. Mei, M. Fan, R. Lu, R. Du, K. Chen, J. Yao, Z. Jiang and H. Li, *Inorg. Chem.*, 2020, **59**, 3562–3569.
82 K. Motokura, S. Ding, K. Usui and Y. Kong, *ACS Catal.*, 2021, **11**, 11985–12018.
83 X. F. Zhou, *RSC Adv.*, 2014, **4**, 28029–28035.
84 W.-J. Zhou, B. Albela, M.-Y. He and L. Bonneviot, *Polyhedron*, 2013, **64**, 371–376.
85 (*a*) CCDC 2495739: Experimental Crystal Structure Determination, 2025, DOI: 10.5517/ccdc.csd.cc2ps0q7; (*b*) CCDC 2495740: Experimental Crystal Structure Determination, 2025, DOI: 10.5517/ccdc.csd.cc2ps0r8; (*c*) CCDC 2495857: Experimental Crystal Structure Determination, 2025, DOI: 10.5517/ccdc.csd.cc2ps4j5.